Omnimodal topological polarization of bilayer networks: theoretical characterization in the Maxwell limit and experiments on a 3D-printed prototype

Mohammad Charara,^{1,*} James McInerney,^{2,*} Kai Sun,² Xiaoming Mao,^{2,†} and Stefano Gonella^{1,‡}

¹Department of Civil, Environmental, and Geo- Engineering,

University of Minnesota, Minneapolis, MN 55455, USA

²Department of Physics, University of Michigan, Ann Arbor, MI 48109, USA

(Dated: April 29, 2022)

Two-dimensional, critically-coordinated mechanical networks can exhibit topologically polarized modes that are exponentially localized to a particular edge; however, the coupling of such in-plane deformation to out-of-plane curvature remains largely unexplored. Here, we investigate a class of mechanical bilayers as a model system for designing topologically protected edge modes beyond the in-plane paradigm. In particular, we apply the spring-mass modeling framework, familiar to topological mechanics, to bilayers with mirror-symmetric layers adjoined via a particular choice of interlayer connections, and we show that a unified topological index can be defined, thereby characterizing the *omnimodal topological polarization* of both in-plane and out-of-plane modes. Furthermore, we quantify the manner in which these flexural modes are lifted to finite frequencies while remaining localized when the harmonic springs are replaced by elastic beams. This analysis is supported by experiments conducted on a prototypical lattice fabricated via additive manufacturing where we confirm both the edge selectivity and the frequency selectivity of the mechanical structure.

I. INTRODUCTION

Topological phases of matter have properties that are characterized by a topological invariant, rather than by symmetry breaking alone. Examples include electronic topological insulators where the band structure of the bulk ensures the existence of topologically protected, conducting states on the boundary [1, 2]. Similar topological phases exist for a variety of mechanical systems which can be utilized for the design of mechanical metamaterials with one-way propagating elastic waves [3–8], including elastic plates where in-plane extensional modes couple to out-of-plane flexural modes [9-15]. These topological insulator analogues are a subset of more general topological mechanical metamaterials [16, 17], which also include systems that possess topologically protected static properties such as zero-frequency edge modes and forcebearing modes [18-26]; however, the coupling between inplane and out-of-plane degrees of freedom for such zero modes remains to be explored.

Maxwell networks are discrete mechanical systems that possess equal numbers of degrees of freedom and energetic constraints, such as networks of point masses connected by harmonic springs [27, 28] and fiber networks relevant for biological structures [29–31]. Such systems possess an average coordination number equal to twice the dimension of their embedding space, which places them near onset of the rigidity transition [27, 32]. Nonetheless, this class of materials can still exhibit various modes of deformation such as nonlinear lattice reconfigurations [33, 34], mechanical solitons [35, 36], me-

chanical Weyl modes [23–25, 37], and of present interest: exponentially localized zero frequency modes. Interestingly, an excess of these modes can be localized to a particular boundary, a phenomenon known as *topological polarization*, whereby opposite sides of the material are rendered floppy or stiff [18–26].

Although the in-plane, topologically polarized modes of two-dimensional Maxwell lattices are well understood, fundamental questions remain about the mechanics of two-dimensional Maxwell lattices embedded in threedimensional space. Flexural modes dominate the lowenergy mechanical response of thin plates due to the relative scaling of their bending and stretching moduli [38]. This feature can be manipulated for the deployment and transformation of mechanical structures by programming particular flexural modes into the sheet, such as the rigid folding modes of origami metamaterials [39-41]. However, triangulated origami, which lies at the Maxwell point, possesses a hidden symmetry that prohibits its topological polarization [42]. While this hidden symmetry can be broken by introducing an equal number of quadrilateral faces and holes [43], thereby yielding topologically polarized Maxwell kirigami [44], these quadrilateral faces exhibit additional low-energy modes, due to bending of the faces [45, 46], which are not necessarily localized.

Alternatively, mechanical bilayers could be used to generate topologically polarized flexural edge modes by utilizing the well-developed topological phase space of two-dimensional Maxwell lattices [22]. Indeed, bilayers composed of two kagome layers with mismatched characteristics (polarized and unpolarized) exhibit edgelocalized, finite-frequency modes due to the coupling of in-plane and out-of-plane mechanics enforced by the compatibility constraints at the interface between the layers [47]. However, in contrast to the planar kagome lattice, an analytical characterization of topologically po-

^{*} Authors share equal contribution.

[†] maox@umich.edu

[‡] sgonella@umn.edu

larized edge modes in Maxwell bilayers is missing; such insight could provide guidance on the construction of a bilayer which exhibits edge modes that can be actuated from both in-plane and out-of-plane excitations, a condition that we refer to as *omnimodal polarization*. In addition, the observation of these edge modes at finite frequencies is a hallmark of experimental realizations of Maxwell lattices, such as the planar kagome lattice [48], where stiffness in the physical joints lifts the zero modes to finite frequencies [49–51] and can move edge modes into the bulk [52]. This offers a new platform for the edge transport of topological flexural modes, distinct from existing topological insulator analogues.

In the present manuscript, we introduce a family of mechanical structures, referred to as mirror-symmetric kagome bilayers, and we use analytical calculations, numerical simulations, and experimental observations to investigate their topologically polarized edge modes, with particular emphasis on the out-of-plane deformations. We first consider the system as an idealized Maxwell lattice and show that the mirror symmetry between the layers, along with a particular choice of interlayer connections, controls the topological polarization of the bilayer. Next, we replace the harmonic springs of the Maxwell bilayer with elastic beams that meet at rigid joints and explore the dependence of the mode frequency as well as the mode localization on the thickness of these beams. Finally, we use laser vibrometry experiments to elucidate the topologically polarized edge modes on a 3D-printed bilayer prototype and support these results with numerical simulations.

II. RESULTS AND DISCUSSION

A. Topological polarization of Maxwell bilayers

Maxwell bilayers are critically-coordinated spring-mass networks which are embedded in three-dimensional space and are periodic along two of these directions. Here, we review the topological mechanics of two-dimensional distorted kagome lattices and then introduce a family of Maxwell bilayers that are composed of mirror copies of topologically polarized kagome lattices. We show that the symmetry between the layers, along with a particular choice of interlayer connections and small height modulations, yields zero modes, including both in-plane and out-of-plane displacements, that topologically polarize to the same edge as they do in the planar lattice at large wavenumber.

Consider the planar, distorted kagome lattice shown in Fig. 1A. The unit cell of this network is composed of point masses at the three vertices, $\mathbf{r}_1 = (0, 0)$, $\mathbf{r}_2 = (1, 0.3)$, and $\mathbf{r}_3 = (0.5, 3 + 0.6)$, and harmonic springs along the six edges, \mathbf{r}_{ij} , connecting the vertices. Each cell is related to its neighbors by the lattice vectors, $\mathbf{\ell}_1 = (2, 0)$ and $\mathbf{\ell}_2 = (1, 3)$, so that the position of vertex i in cell $\mathbf{n} = (n_1, n_2)$ is: $\mathbf{r}_i(\mathbf{n}) = \mathbf{r}_i + n_1\mathbf{\ell}_1 + n_2\mathbf{\ell}_2$. Impor-

tantly, each vertex possesses two linear degrees of freedom whereas each edge provides one linear constraint so that the periodic lattice is critically coordinated. Note that the analysis in this section is scale-independent so that the lengths are written in dimensionless units.

The mechanical response of such a spring-mass network is characterized by its normal modes. The infinitesimal displacements, \mathbf{u}_i and \mathbf{u}_i , of vertices i and i, respectively, extend the spring adjoining these vertices to firstorder, \hat{r}_{ij} ($\mathbf{u}_i = \mathbf{u}_i$), thereby leading to a restoring force directed along their shared edge, \hat{r}_{ij} , which causes the masses to oscillate about their equilibrium position with frequency ω . The linear operator, **C**, called the *compat*ibility matrix, maps the vector of all displacements, U, to the vector of all extensions, E, so that such oscillations correspond to the normal modes, $\mathbf{D}\mathbf{U} = \omega^2 \mathbf{M}\mathbf{U}$, of the dynamical matrix, $\mathbf{D} = \mathbf{C}^T \mathbf{KC}$, where \mathbf{M} (\mathbf{K}) is a diagonal matrix of point masses (spring constants). For identical point masses, m, and spring constants, k, these dynamics can <u>b</u> e non-dimensionalized by introducing the timescale m/k, in which case the mass and spring constant matrices are given by the identity matri $ces \mathbf{M} = \mathbf{K} = \mathbf{1}.$

For periodic networks, such as the kagome lattice, these normal modes are Bloch periodic in the bulk. Hence, the compatibility matrix can be diagonalized into blocks, $\mathbf{C}(\boldsymbol{\xi})$, for each wavevector, $\boldsymbol{\xi} = (\xi_1, \xi_2)$, by Fourier transforming the unit cell over the cell indices so that an intercellular bond belonging to the cell \mathbf{n} (e.g., the dashed bonds in Fig. 1A) carries a Bloch factor, $e^{i\mathbf{n}\cdot\boldsymbol{\xi}}$. The corresponding displacements vary between cells as $\mathbf{U}(\mathbf{n}) = \mathbf{U}e^{i\boldsymbol{\xi}\cdot\mathbf{n}}$, where \mathbf{U} is an eigenvector of the Blochperiodic dynamical matrix $\mathbf{D}(\boldsymbol{\xi}) = \mathbf{C}(\boldsymbol{\xi})^{\dagger}\mathbf{KC}(\boldsymbol{\xi})$, with \dagger denoting Hermitian conjugation.

Maxwell lattices can exhibit a particular type of nor-

mal modes, called *zero modes*, which do not stretch the springs and therefore lie in the nullspace of the compatibility matrix. This nullspace is non-empty at wavevectors for which the determinant of the square compatibility matrix vanishes: det $\mathbb{C}(\xi) = 0$. In general, this determinant is a Laurent polynomial in the Bloch factors, c_{T_p} , c_{T_p} , c_{T_p} , c_{T_p} , c_{T_p} , where the highest (lowest) order of the sum is given by the number of intercellular bonds connecting to the next (previous) cell and c_{T_p} , c_{T_p} are real-valued coefficients that depend on the lattice geometry. The symmetric gauge, for which there are an equal number of forward and backward intercellular bonds (illustrated by the solid lines of the unit cell in Fig. 1A), is

The roots of this polynomial are generically at complex wavevectors which correspond to zero-frequency edge modes. For any value of the transverse wavenumber, ξ_1 , the determinant of the compatibility matrix in the distorted kagome lattice vanishes at two distinct ξ_2 due to the two intercellular bonds in the \mathbf{f}_2 direction. Since the modes vary between cells according to Bloch's theorem, the imaginary part of the wavenumber, $\kappa_2 = \text{Im } \xi_2$, specifies the decay rate which determines how the mode am-

used to eliminate any overall phase factors [18, 21, 53].

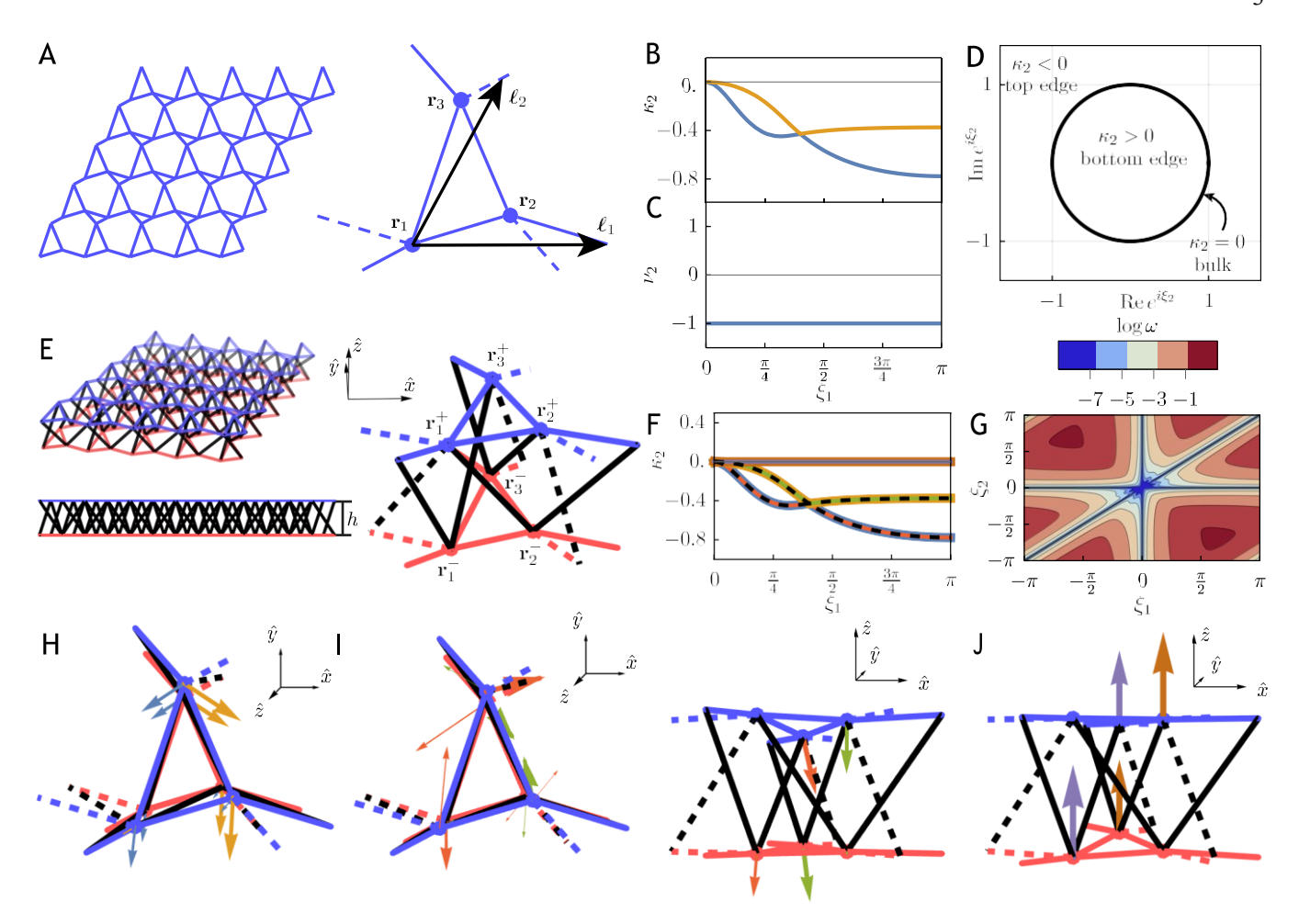


FIG. 1. spring-mass model for Maxwell bilayers. (A) Topological kagome lattice and its unit cell with vertex positions, \mathbf{r}_i and lattice vectors $\mathbf{\pounds}_i$. The solid lines indicate the bonds of the cell defined in the symmetric gauge while the dashed lines indicate bonds that belong to adjacent cells. (B) Decay rate, κ_2 , and (C) winding number, ν_2 , for the distorted kagome lattice shown in panel A. (D) Illustration of the contour taken over the bulk modes, $\kappa_2 = 0$, that is used to compute the winding number. (E) Mirror symmetric kagome bilayer with interlayer separation h between two copies (distinguished by blue and red bonds) of the topological kagome lattice in panel A, vertex positions \mathbf{r}_i^{\pm} , and interlayer connections (indicated by black bonds). (F) Decay rate and (G) eigenfrequency of the lowest band, ω , of the coplanar bilayer in panel E, where the dashed lines in panel F are exactly the decay rates of the planar modes and the zero decay rate lines correspond to the lines of bulk modes in panel G. Illustration of the (H) symmetric in-plane modes, (I) antisymmetric, and (J) vertex-pair out-of-plane modes.

plitude accumulates, $|\mathbf{U}(n_2)| = e^{-in_2 \kappa_2}|$. These decay rates are computed over the real values of the transverse wavenumber, ξ_1 , in Fig. 1B, showing that this particular geometry has both of its zero modes localized to the top edge (which corresponds to positive values of n_2) when subjected to periodic boundary conditions in the \mathbf{f}_1 direction. This means that the the top edge is inherently floppy relative to the bottom edge. More general two-dimensional Maxwell lattices exhibit zero modes at one $\xi_2 = \xi_2(\xi_1)$ per intercellular bond in the \mathbf{f}_2 direction, but interestingly always possess two zero modes in the continuum limit [53, 54].

The localization of these zero modes is topologically protected by an integer-valued invariant called the *winding number* [18]. This quantity counts the relative number of zeros and poles of the determinant of the compat-

ibility matrix within a region by integration of its phase over the contour enclosing the region [55]. In particular, the contour can be taken over the bulk modes, $\kappa_2 = 0$, which bound the modes localized to the top edge, $\kappa_2 < 0$, and those localized to the bottom edge, $\kappa_2 > 0$, as illustrated in Fig. 1D. Thus, for any value of the transverse wavenumber, ξ_1 , the winding number,

$$\nu_2(\xi_1) = \frac{1}{2\pi} \int_{-\pi}^{+\pi} d\xi_2 \frac{\partial}{\partial \xi_2} \operatorname{Im} \log \det \mathbf{C}(\xi_1, \xi_2), \quad (1)$$

determines the relative number of zero modes localized to each edge. In the symmetric gauge, this determinant has an equal number of roots and poles at the origin [18, 21, 53] so that an unpolarized kagome lattice, which has one zero mode localized on each of the two

opposing edges, has a winding number of $v_2 = 0$. For the polarized kagome lattice with strictly negative decay rates, the winding number is $v_2 = 1$ for every transverse wavenumber, as shown in Fig. 1C. Note that the winding number is undefined when the contour crosses zero modes such as the rigid body modes at $\xi_1 = 0$ as well as bulk modes referred to as Weyl points where the topological invariant can undergo a jump discontinuity [37].

This framework for topological mechanics can be applied to any Maxwell lattice, such as the symmetric kagome bilayer shown in Fig. 1E. This particular bilayer is composed of mirror copies of the polarized kagome lattice shown in Fig. 1A (distinguished by blue and red edges) separated by interlayer height, h = 0.75. The positions of the six point masses in the unit cell can be written in terms of the planar positions: $\mathbf{r}_{i}^{\pm} = \mathbf{r}_{i} \pm \mathbf{r}_{i} \not\equiv \mathbf{r}_{i}$, where +(-) specifies a mass in the upper (lower) layer. Since these masses now possess three linear degrees of freedom, six additional springs are added to the unit cell

to make the bilayer critically coordinated, as indicated by the black edges in Fig. 1E, which connect the vertices in pairs between the upper and lower layers,

$$\mathbf{r}_{1}^{+} \leftarrow \rightarrow \mathbf{r}_{2}^{-} \leftarrow \rightarrow \mathbf{r}_{1}^{+}(1,0),$$

$$\mathbf{r}_{2}^{+} \leftarrow \rightarrow \mathbf{r}_{3}^{-} \leftarrow \rightarrow \mathbf{r}_{2}^{+}(-1,1),$$

$$\mathbf{r}_{3}^{+} \leftarrow \rightarrow \mathbf{r}_{1}^{-} \leftarrow \rightarrow \mathbf{r}_{3}^{+}(0,-1),$$
(2)

where the final vertices lie in adjacent cells denoted by $\mathbf{n} = (n_1, n_2)$. While alternative choices of these inter-

layer connections can be made, this particular connectivity yields a predictable topological phase space.

The corresponding Bloch-periodic compatibility matrix maps in-plane () and out-of-plane () degrees of freedom in the upper (+) and lower (_) layers to constraints on the upper (+), lower (_), and interlayer (+) bonds:

$$\mathbf{E}^{\pm} = \mathbf{C}_{\mathbf{I}}^{-} \quad \mathbf{C}_{\mathbf{I}}^{+} \quad \mathbf{C}_{\mathbf{I}}^{+}$$

Importantly, the mirror symmetry implies that the intralayer, in-plane constraints are equal for each layer, $C_{I} = C_{I}^{+}$ so that the two zero modes of the planar lattice remain zero modes of the bilayer. The characterization of the remaining modes depends on the relative heights of the vertices within each layer.

For *coplanar* bilayers, where the upper and lower layers are flat, the intralayer, out-of-plane constraints are trivially satisfied, $\mathbf{C}_{\perp}^{-}\mathbf{U}_{\perp}^{-} = -\mathbf{C}_{\perp}^{+}\mathbf{U}_{\perp}^{+} = \mathbf{0}$, so that the out-of-plane displacements are only constrained by the interlayer connections which couple individual pairs of vertices to one another. Consequently, coplanar, mirror symmetric Maxwell bilayers have three types of zero modes. The first two types exist at the same wavevectors as the zero modes of the planar lattice, where one

type, U_{sym}, has symmetric in-plane with vanishing outof-plane displacements and the other type, U_{asym}, has antisymmetric in-plane with non-vanishing out-of-plane displacements,

$$\mathbf{U}_{\text{sym}} = (+\mathbf{U}_{\text{I}}, \mathbf{o}, +\mathbf{U}_{\text{I}}, \mathbf{o}), \tag{4}$$

$$\mathbf{U}_{\text{sym}} = (+\mathbf{U}_{\text{I}}, \mathbf{o}, +\mathbf{U}_{\text{I}}, \mathbf{o}), \qquad (4)$$

$$\mathbf{U}_{\text{asym}} = (+\mathbf{U}_{\text{I}}, \mathbf{U}^{-}, -\mathbf{U}_{\text{I}}, \mathbf{U}^{+}), \qquad (5)$$

where $\mathbf{U}_{_{|}}^{_{+}} = \mathbf{U}_{_{|}}^{_{-}}$ due to asymmetry of the interlayer connections. The third type of zero mode, \mathbf{U}_{pair} is the strictly out-of-plane displacement of any pair of vertices that are coupled by the interlayer constraints,

$$\mathbf{U}_{\text{pair}} = (\mathbf{o}, \boldsymbol{\delta}_{i}^{-}, \mathbf{o}, \boldsymbol{\delta}_{i}^{+}), \tag{6}$$

where $\boldsymbol{\delta}_{i}^{-} = \boldsymbol{\delta}_{j}^{+}$ are the isolated out-out-of plane displacements of vertices i and j in the lower and upper layers respectively, which are connected via interlayer bonds. These vertex-pair modes exist at wavevectors for which the displacements of vertices that are coupled by interlayer connections do not accumulate: $\mathbf{o}_{i}(\mathbf{n}^{t}) = \mathbf{o}_{i}(\mathbf{n}^{t})$

 δ_i . Note that Maxwell bilayers with larger unit cells can exhibit a similar type of mode which couples more than two vertices to one another provided that the interlayer connections are of the form given in Eqn. (2).

Since the mirror-symmetric kagome bilayer has six total intercellular bonds along the $\mathbf{\mathcal{E}}_2$ direction (two from each layer and another two adjoining the layers together), it can exhibit up to six zero modes localized to a single edge for any value of the transverse wavenumber ξ_1 . Both the symmetric mode in Eqn. (4) and the antisymmetric mode in Eqn. (5) vary between cells according to the wavevectors of the planar lattice zero modes so that their decay rates are doubly degenerate, as shown in Fig. 1F. The two symmetric and antisymmetric modes at $\xi_1 = \pi$ are respectively illustrated in Figs. 1H and I, matching the color of their respective decay rates. The vertex-pair modes in Eqn. (6) are given by $\delta^3 = \delta^1$ for $\xi_2 = 0$ and $\delta_2 = \delta_3$ for $\xi_2 = \xi_1$, as illustrated in Fig. 1J. Note that these can be both bulk modes, as shown in by the lines of zero frequency modes of the lowest band in Fig. 1G where there exists a third line corresponding to $\boldsymbol{\delta}^- = \boldsymbol{\delta}^+$ at $\boldsymbol{\xi}_1 = 0$, as well as boundary modes. Importantly, the presence of these bulk modes at all transverse wavenumbers invalidates the winding number.

The introduction of a vertex-dependent height modulation, η_i , as illustrated in Fig. 2A, breaks the geometry singularity that gives rise to these bulk modes. The corresponding vertex positions are computed $\mathbf{r}_{i}^{\pm} =$ $\mathbf{r}_i \pm (\frac{h}{2} + \eta_i)\hat{\mathbf{z}}$, and the intralayer edges now constrain out-of-plane displacements, $\mathbf{C}_{\perp} = -\mathbf{C}_{\perp}^{-} = \mathbf{o}$, so that the wavevectors of the zero modes cannot admit antisymmetric solutions of the form in Eqn. (5) and there are no lines of bulk modes due to the vertex-pair modes of the form in Eqn. (6); thus, the degeneracy of the zero modes is broken. Interestingly, the decay rates change by an

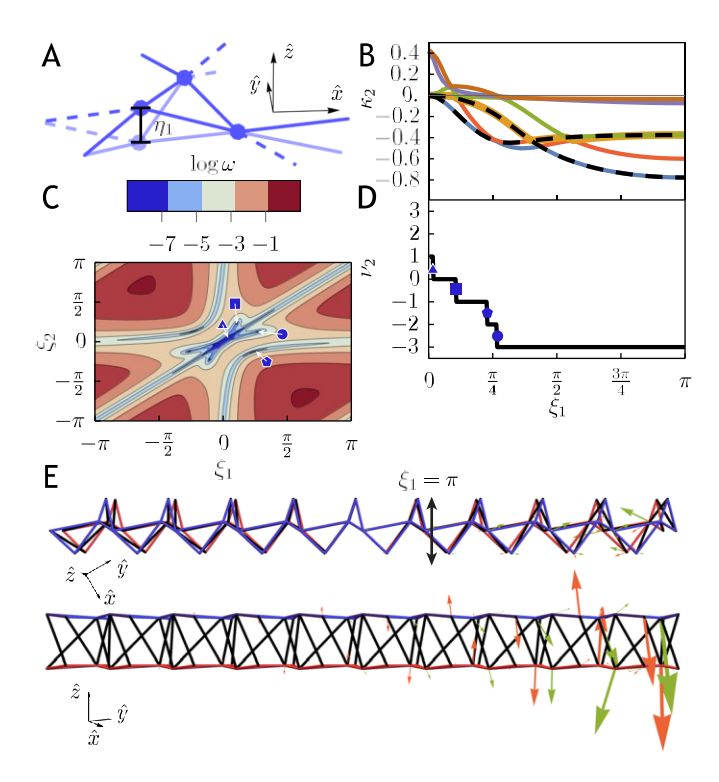


FIG. 2. Mirror symmetric, noncoplanar kagome bilayer. (A) Height modulation, η_1 , makes the layers noncoplanar. (B) Decay rates, κ_2 , and (D) winding number, ν_2 , as a function of the transverse wavenumber, ξ_1 . The black dashed lines are the decay rates for zero modes of the planar kagome. (C) Eigenfrequencies of the lowest band with Weyl points that yield discontinuities in the winding number in panel D. (E) Illustration of the localization of the two strongly decaying modes in panel B (with corresponding colors) at $\xi_1 = \pi$, which couple in-plane and out-of-plane displacements.

amount that is dependent on the size of the height modulation so that at large transverse wavenumber, the four edge modes remain localized and the bulk modes localize to one side of the bilayer with a low decay rate.

For the particular choice of $\eta_1 = 0.1$ and $\eta_2 = \eta_3 = 0$, all six of the zero modes of the kagome bilayer localize to the top edge at large transverse wavenumber. This is shown by the negative decay rates, $\kappa_2(\xi_1 = \pi) < 0$, in Fig. 2B and the winding number, $\nu_2(\xi_1 = \pi) = -3$, in Fig. 2D. In contrast to the lines of bulk modes in the coplanar bilayer, the noncoplanar bilayer exhibits Weyl points (see Fig. 2C) at low wavenumber. The localization of the two strongly localized, non-planar modes are illustrated in Fig. 2E. Thus, this construction of mirror-symmetric kagome bilayers fully polarizes the lattice so that the top is floppy and the polarization is omnimodal due to the in-plane and out-of-plane characteristics of these modes.

The analysis of the topologically polarized, mirrorsymmetric kagome bilayer presented here can be extended to bilayers composed of topological square lattices [22, 37], bilayers without mirror symmetry which do not exhibit strictly in-plane modes, and bilayers with

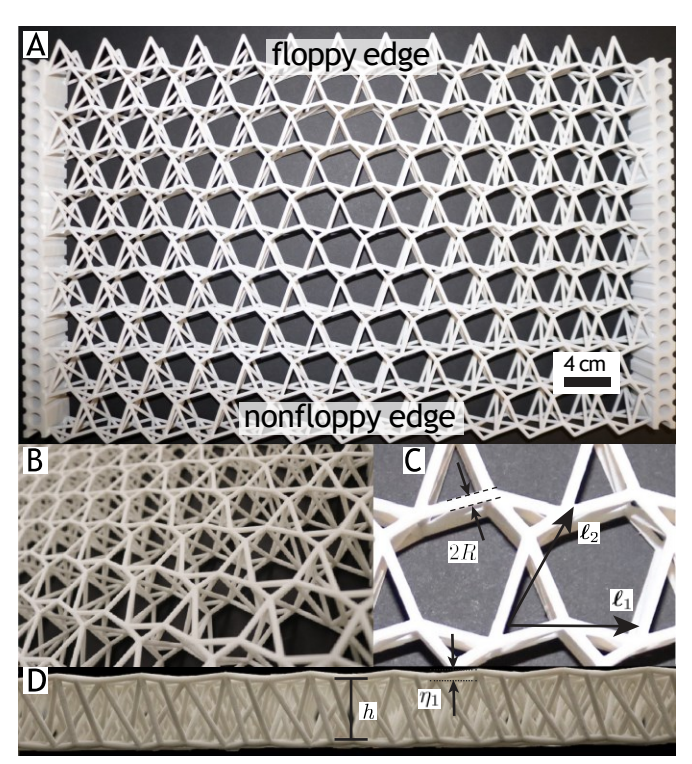


FIG. 3. 3D-printed structural lattice: (A) Top-down and (B) angled views of the symmetric kagome bilayer introduced in Fig. 1 constructed via SLS and composed of glass-fiber-reinforced nylon beams with radius R = 1.5 mm. The lattice geometry is proportional to that of the spring-mass model. (C) Close-up of the lattice unit cell with lattice vectors $\pounds_1 = 2(2, 0, 0)$ cm and $\pounds_2 = 2(1, 3, 0)$ cm. (D) Front view of the bilayer with layer height separation h = 3 cm and height modulation $\eta_1 = 2$ mm.

interlayer connections that yield flat bands in the coplanar limit (see Appendix A). Thus, investigations of less restrictive geometries could provide greater control over the presence of bulk modes and exhibit more strongly polarized flexural modes.

B. Edge modes in structural bilayers: supercell analysis simulations

We turn our attention to realizing topological behavior of the bilayer in a structural lattice constructed via additive manufacturing. Here, we model the bilayer supercell as a network of interconnected Timoshenko beams, and calculate its band diagram and mode shapes, thereby revealing the presence of polarized modes (with both inplane and out-of-plane characteristics) below the bulk band. However, two of the six polarized edge modes predicted in the spring-mass model rise into the bulk under beam kinematic conditions. We show that these modes localize for beams with vanishingly small radii, where the relatively low cost of beam bending results in the recovery of features of the ideal Maxwell conditions, although

never reaching them.

We design a kagome bilayer featuring a geometry and connectivity closely matching that of the spring-mass lattice studied in the previous section, and fabricate the 10×13 -cell prototype shown in Fig. 3 via selective laser sintering (SLS) with glass-fiber-reinforced nylon (Stratasys Nylon 12 GF - Young's modulus = 2.896 GPa - see Materials and Methods). In the structural lattice, the springs connecting the sites are replaced with beams of radius R=1.5 mm, whose mass is distributed along the length of the beam, rather than lumped at the sites. The lattice features an interlayer height h=3 cm and modulation at site 1 $\eta_1=2$ mm. Note that constraints are printed on the left and right edges of the lattice to act as clamping sites in the experiments.

The bonds of the structural lattice can be modeled as 3D Timoshenko beams [56, 57] capable of undergoing axial, flexural, shear, and torsional deformations. While in the spring-mass model connections between sites could be interpreted as perfect hinges, so that we refer to them as ideal Maxwell, here the beams are joined at internal clamps: the relative angles formed by beams meeting at a joint are preserved during deformation. In the finite element method (FEM) framework (see Materials and Methods), each lattice bond is discretized multiple beam elements, each featuring six degrees of freedom per node: three nodal displacements \mathbf{u}_m - one axial and two lateral (in orthogonal planes) - and three cross sectional rotations θ_m – representing two tilts and a twist – where the subscript m is the node index along the beam (see Appendix D).

The dynamical matrix of a single beam element is given by $\mathbf{D}_b = {}^{\mathsf{T}}\mathbf{B} \mathbf{K} \mathbf{B} dL$, where L is the length of the beam element, **B** is a matrix of derivatives of the shape functions, which approximate the compatibility relations within one element, and K_b is a diagonal constitutive matrix of elastic constants, featuring rigidity contributions for axial deformation (scaling with R^2), lateral deflection (scaling with R^4) [encompassing the effects of, both, shear and bending deformability encoded in the beam model], and torsional deformation (scaling with R^4). Dynamical matrices of each individual beam are assembled into a global dynamical matrix for the entire system, which is used for computational analysis. Note that, for each discretized beam element, B plays a role analogous to a single row of C in the spring-mass counterpart, for a single bond.

We construct a supercell to calculate the band diagram of the structural lattice by connecting 10 unit cells, discretized using 3D Timoshenko beam elements, in the $\mathbf{\pounds}_2$ direction with free boundary conditions at the ends, and Bloch-periodic boundary conditions with respect to wavenumber ξ_1 in the $\mathbf{\pounds}_1$ direction. We extract the Bloch-reduced arrays of generalized nodal displacements $\tilde{\mathbf{U}}$ and cross-sectional rotations $\tilde{\mathbf{\Theta}}$ in the supercell as the modes of $\tilde{\mathbf{D}}_b(\xi_1)$ $\tilde{\mathbf{U}}$ $\tilde{\mathbf{\Theta}}$ = $\omega^2 \tilde{\mathbf{M}}_b(\xi_1)$ $\tilde{\mathbf{U}}$ $\tilde{\mathbf{\Theta}}$, where $\tilde{\mathbf{D}}_b(\xi_1)$ $[\tilde{\mathbf{M}}_b(\xi_1)]$ is the dynamical [mass] matrix of the supercell

under Bloch conditions.

The resulting supercell band diagram is shown in Fig. 4A. We seek the edge modes among the low-frequency modes that fall below the bulk band, and towards the edge of the Brillouin zone, in analogy with the scenario described in Ref. [47] – the relevant portion of the branches are plotted in black. The mode shapes of the lowest four modes at $\xi_1 = \pi$ are shown so that the in-plane deformation is shown with color intensity proportional to displacement along y (the Cartesian direction normal to the open boundaries of the supercell and lattice) and the out-of-plane deformation with color proportional to displacement along z.

Both in-plane and out-of-plane deformation exhibit strong localization at the top end of the supercell, with a comparable decay rate. This means that the nodal displacements $\tilde{\mathbf{U}}_{n_2}$ of cell n_2 in the supercell increase exponentially towards the top, $n_2 = 10$. The strength of localization is effectively highlighted by the dimensionless mode density,

$$\rho_{n_2} = \begin{array}{c} & \frac{\tilde{\mathbf{U}}_{n_2} \cdot \tilde{\mathbf{U}}_{n_2}}{\tilde{\mathbf{U}} \cdot \tilde{\mathbf{U}}}, \\ & \tilde{\mathbf{U}} \cdot \tilde{\mathbf{U}} \end{array}$$
(7)

which quantifies the contribution of nodal displacements in each cell of the supercell, as shown for the lowest six modes at wavenumber $\xi_1 = \pi$ in Fig. 4D. The most striking observation is that all four modes below the bulk band are localized. This is a considerable qualitative improvement over the results presented in Ref. [47], in which only two polarized edge modes were found and, more importantly, where the overall signature of polarization in the flexural response was significantly milder. Moreover, the localization of these modes highlights that the top and bottom edges of this bilayer serve as the floppy and nonfloppy edges, respectively, consistent with the predictions from the spring-mass model. Note that $\tilde{\mathbf{U}}_{n_2}$ also includes the displacement of nodes on the boundary of the supercell which were previously reduced due to application of periodic boundary conditions.

In contrast to the spring-mass lattice, where all six zero modes localize, here, modes five and six show no signature of localization. This suggests that the structural bilayer lattice is not immune from a certain degree of dilution of the topological polarization observed in its ideal Maxwell counterpart. This dilution is a direct result of the non-ideality of the hinges, enforced by the beam internal clamp boundary conditions, which invoke flexural mechanisms whose energy cost overwhelms the response of the system. Moreover, in response to the relaxation of ideal conditions, each of the six zero modes rises to finite frequencies by different amounts when compared to the bulk modes; this effect should to be correlated to the strength of their polarization, although further work is needed to confirm this hypothesis [52].

Studying the dependence of the mode landscape as a function of the strength of the flexural mechanisms of the

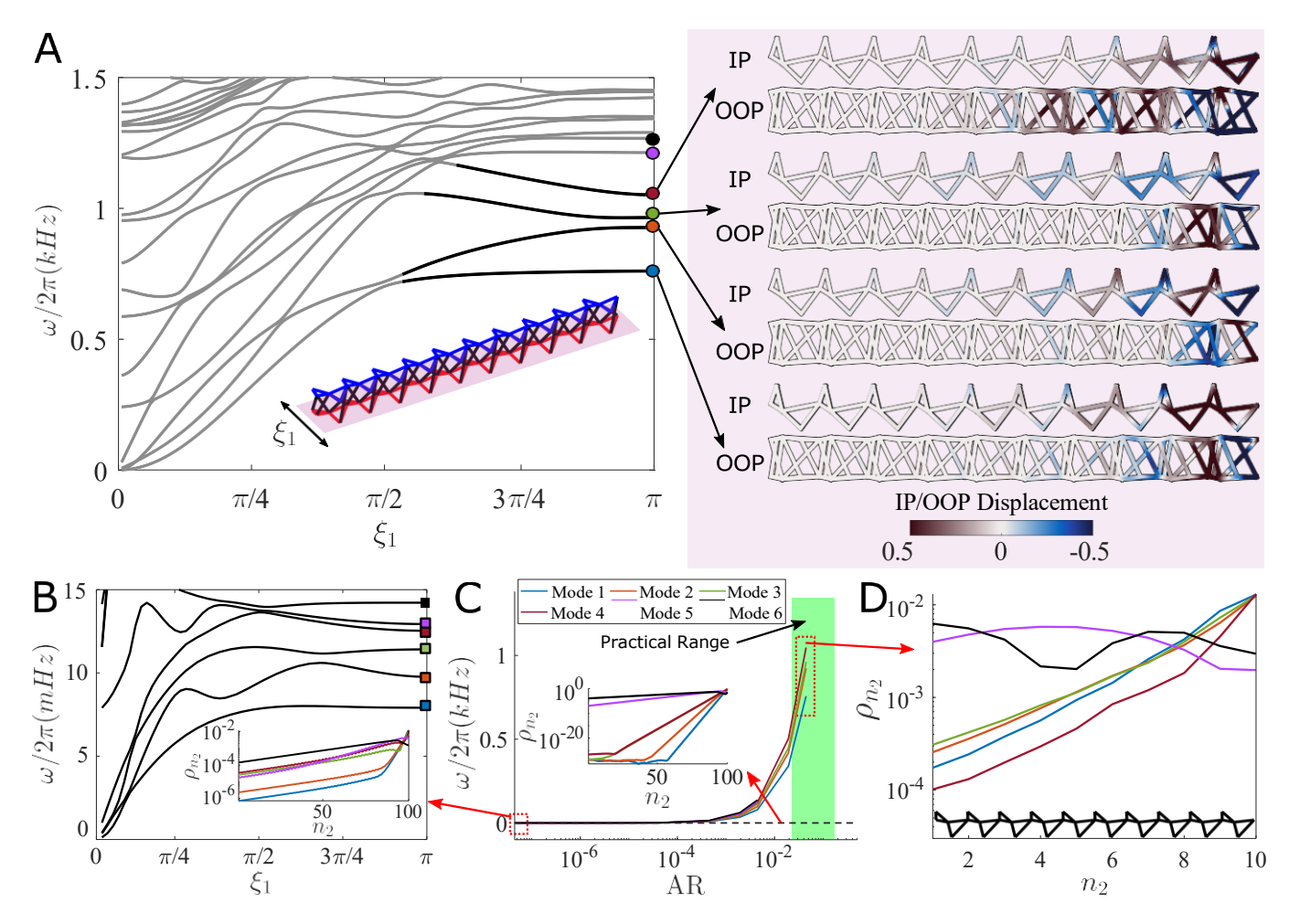


FIG. 4. (A) Band diagram of a 10-unit bilayer supercell (angled view shown in the inset), calculated using 3D Timoshenko beam finite element discretization; mode shape of modes 1-4 at $\xi = \pi$, with in-plane (IP) and out-of-plane (OOP) deformation plotted with color intensity proportional to displacement along y and z, respectively (each IP and OOP mode shape is normalized by the highest displacement value of that data set) - here y is chosen to represent in-plane displacement due to it being normal to the top and bottom edges; (B) supercell band diagram for low aspect ratio (AR) beams, (approaching the spring-mass model limit) showing six decaying modes separated from the bulk band, whose decay rates at $\xi = \pi$ - highlighted by the square markers - are shown in the mode density ρ_{n2} vs. cell index plot in the inset); (C) frequency of the six lowest modes as a function of AR, with inset showing the mode density ρ_{n2} vs. cell index plot for the spring-mass system at $\xi = \pi$ (the legend here also applies to panel B and D); (D) ρ_{n2} vs. cell index for the first 6 modes of the supercell in panel A [with AR value compatible with manufacturing constraints] (highlighted be the circle markers), showing four decaying modes and two bulk modes. The green region in panel B highlights the practical region of AR - beam with ARs below are filaments outside the realization of most additive manufacturing methods, and those above intersect each other and become too thick to approximate with beam theory.

beams provides insight in how the mechanics of the structural lattice deviate from those of the ideal Maxwell case. Given the different scaling of axial and bending stiffness with the beam radius R (the ratio of the former to the latter is $1/R^2$), the energy cost associated with flexural effects becomes negligible as the beam thickness decreases. For this reason, a good metric for the strength of the flexural mechanisms is the beam aspect ratio, AR = R/L, where here L is the length of the shortest bond in the unit cell. In Fig. 4C we compare the frequency of the topologically polarized modes as a function of AR, monitoring the frequencies of the first six modes (the number of topo-

logical modes predicted by the spring-mass model), until they enter the bulk band and can no longer be identified. As AR decreases, the frequencies tend towards zero, approaching – but never reaching – the spring-mass model conditions. This implies that the energy cost of flexural effects of the beams becomes progressively negligible as $AR \rightarrow 0$, but the kinematics of the internal clamps prevent this limit condition from fully approaching the behavior of an ideal Maxwell lattice.

Interestingly, the band diagram of the low AR case (Fig. 4B) shows that, as we decrease AR, two additional modes drop from the bulk band and become localized,

as confirmed by the mode density shown in the inset. For comparison, decays for the polarized modes of the spring-mass system are shown in the inset of Fig. 4E. Note that a 100 unit-cell supercell was used for both the low-AR and the spring-mass cases due to the low decay rate exhibited by some of the modes, which require a large number of cells to appreciate. To confirm the contrast with the results applicable to our prototype, decay rates for a 100 unit-cell supercell with the geometric characteristics (i.e., AR) of the prototype are shown in the Appendix B; even with the longer supercell we still only observe four localized modes.

C. Wave Propagation in Lattice: Experiments and Full-Scale Simulations

We now experimentally demonstrate the activation of the polarized modes in the bilayer prototype shown in Fig. 3. To this end, we excite the bilayer with, first, in-plane and, later, out-of-plane tone bursts, in the frequency range of the topological edge modes found via supercell analysis, and we perform 3D laser Doppler vibrometer measurements on the lattice sites of the bilayer surface. We verify the proper activation of the desired bulk or edge modes through a morphological inspection of the wavefield data, and a spectral analysis of the transformed wave response in the ξ_{1} ω plane. Furthermore, we ensure that the edge-selective polarization is frequency-selective, thus providing additional evidence that the activated modes are topological in nature. All results are corroborated by full-scale wave propagation simulations of a bilayer lattice, discretized by 3D Timoshenko beams.

The prototype is excited with a 5 cycle burst applied at the tip of the center-most cell of the top and bottom edge, respectively. We excite the lattice at a carrier frequency of 900 Hz which lies in the frequency range 760_1050 Hz, where the topological modes fold and display the highest density of states, to maximize their signatures in the resulting wavefield. The relevant region of the band diagram is shown by the black portions of branches 1-4 in Fig. 4A.

Results for in-plane excitation with a carrier frequency at 900 Hz prescribed at the bottom edge are shown in Figs. 5A and B, and corresponding results for excitation at the top edge are shown in Figs. 5E and F. Snapshots of the resulting out-of-plane wavefields show strong asymmetry between the top and bottom edge excitations: the top edge excitation produces highly localized deformation at that edge, while excitation at the bottom edge produces a bulk-like flexural wave. This corroborates the results from the ideal Maxwell case and the supercell, where the top edge exhibits floppy edge behavior, while the bottom edge is nonfloppy.

We verify activation of the topological modes via spectral analysis of the response. We collect the out-of-plane displacement time histories at evenly spaced points along

the edge where the excitation is applied, perform a 2D discrete Fourier transform (DFT) on this spatio-temporal data matrix, and superimpose the contours of the resulting spectral amplitude surfaces onto the supercell band diagram to infer which modes are predominantly activated. The DFT analysis corroborates the conclusions made from the inspection of the wavefields, supporting the notion of topological polarization. Excitation at the floppy edge produces a spectral signature that is spread across the branches associated with the edge modes. In contrast, excitation of the nonfloppy edge results in activation of longer wavelength modes (at lower values of ξ_1) that belong to the flexural bulk band.

These results are confirmed by simulations performed on a full-scale model of the bilayer lattice, discretized with 3D Timoshenko beam elements (with the same element characteristics used in the supercell analysis). The results for the same excitation conditions used in the experiments (excitation from the nonfloppy edge in Figs. 5C-D, and from the floppy edge in Figs. 5G-H) match the experiments qualitatively, with only a relatively small deviation in frequency that can be attributed to some inevitable discrepancies in material properties between the model and prototype (due to property variability in the material and additive manufacturing process) and to other non-idealities in the geometry of the specimen.

Asymmetric behavior for flexural waves triggered by in-plane excitation is observed in the bilayer presented in Ref. [47], albeit with a significantly milder polarization signature. However, in that case, such asymmetry requires a direct in-plane strain activation of the polarized layer, and is completely lost when the excitation is prescribed out-of-plane. We repeat the experiments with the current bilayer using an out-of-plane force to test the robustness of the asymmetry achievable against changes in the excitation force. We show the resulting wavefields and DFTs for excitations from the nonfloppy (Figs. 5I and J) and floppy (Figs. 5M and N) edges. The results are consistent with their in-plane excitation counterparts: the wavefield snapshots reveal a highly polarized response with displacement localization at the edge when we excite at the floppy edge, and propagation deep into the bulk for excitation at the nonfloppy edge. Again, the DFT plots confirm this dichotomy of the mode activation. The magnitude of this result can be truly appreciated by recalling that the topological character of the bilayer stems from the geometry of its two kagome layers. The dichotomous behavior between the edges documented in Fig. 5 confirms that the coupling provided by the interlayer connections is very effective in transferring the topological character to the flexural modes, yielding omnimodal polarization encompassing both in-plane and out-of-plane behavior. The results are again confirmed by full scale numerical simulations (Figs. 5K, L, O, and P), with the DFTs showing, even more clearly in this case, topological polarization of the edge modes.

For completeness, we assess the frequency selectivity of the polarized behavior by performing experiments and

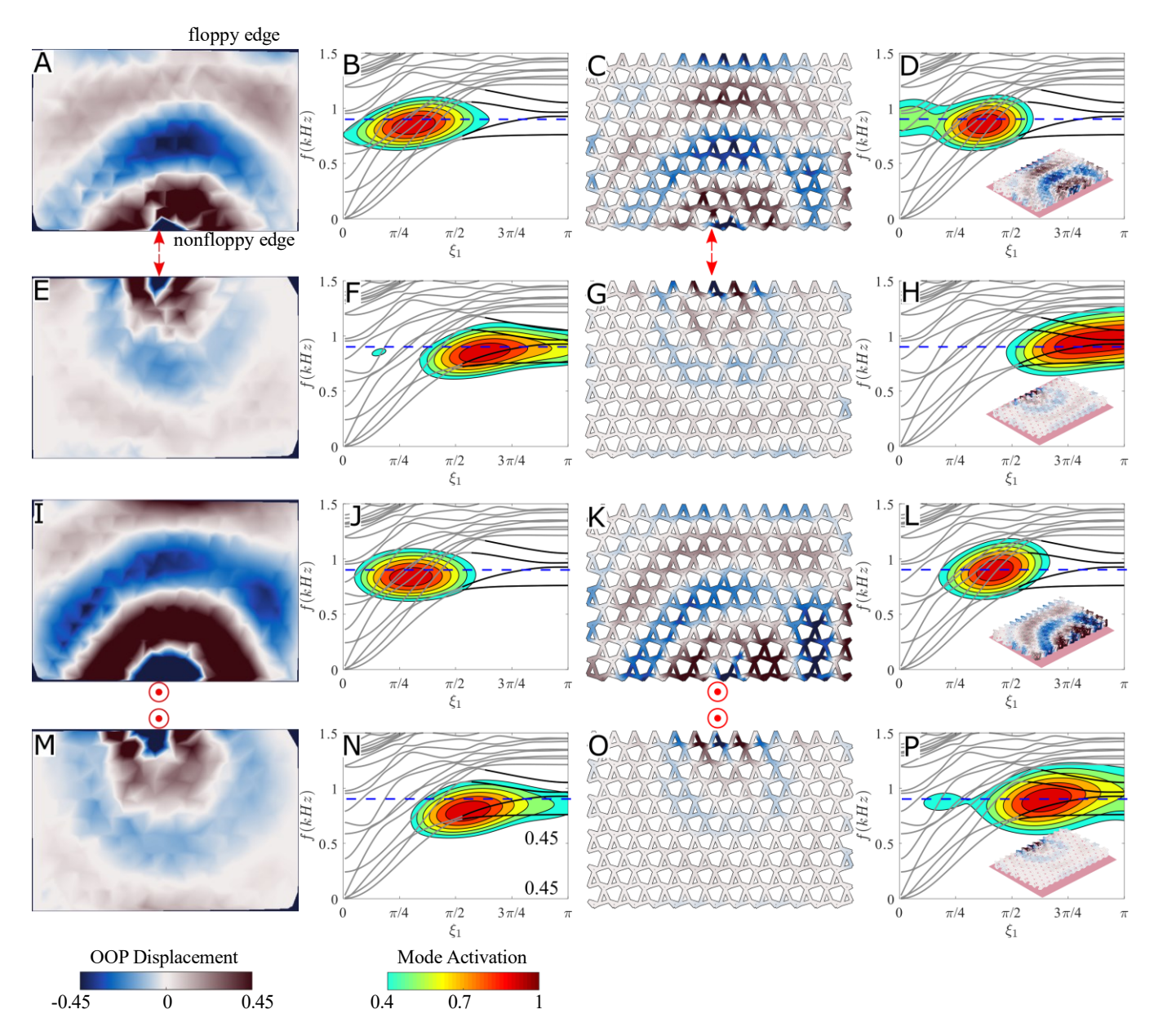


FIG. 5. Wavefield and DFT plots for: experiments (A-B) and simulations (C-D) with an in-plane excitation at the rigid edge, experiments (E-F) and simulations (G-H) with an in-plane excitation at the floppy edge, experiments (I-J) and simulations (K-L) with an out-of-plane excitation at the rigid edge, and experiments (M-N) and simulations (O-P) with an out-of-plane excitation at the floppy edge, all carried out at a carrier frequency of 900 Hz (dashed blue lines). Colorbars in panel M and N apply to all wavefields and contours in the figure, respectively, with the former representing the displacement intensity in the wavefield and the latter highlighting modal activation on the excited edge. While the wavefields capture the signature of wave propagation on the lattice surface, the insets of D, H, L, and P allow to appreciate propagation through the 3D structure of the bilayer. Note that the wavefields and contours are normalized by the highest value in their respective data sets.

simulations at carrier frequencies away from the floppy modes at $\xi = \pi$ (results in Appendix Figs. C). Excitations at 300 Hz reveal nearly identical wavefields when we switch the excitation edge from floppy to nonfloppy, with bulk-like characteristics activated from either side. Although the DFTs from the floppy edge does show some activation of the mode branches endowed with polarized character, the activation occurs at much longer wave-

lengths, where the decay rate of these modes is negligible (making them resemble the bulk modes), overall resulting in bulk-like behavior dominating the response. Experiments performed with a carrier frequency at 1300 Hz also show largely symmetric behavior, although we still see the persistence of some localization when exciting from the floppy edge. This is likely due to the fact that the excitation energy is spread over a band of frequencies due

to the windowing applied to the burst, which causes the edge of the main lobe and the side lobes to excite modes in the topological region.

III. CONCLUDING REMARKS

We have introduced a broad family of topological mechanical metamaterials, referred herein as mirrorsymmetric kagome bilayers, and explored their mechanical response via analytical calculations, numerical simulations, and experimental testing. We have provided an analytical theory of how omnimodal topological polarization arises for coupled in-plane and out-of-plane vibrations of spring-mass Maxwell bilayers. We have also explored how these modes can remain localized at finite frequency when the system is modeled as a frame of elastic beams connected at rigid joints. Finally, we have experimentally verified the existence of this omnimodal polarization via laser vibrometry tests. In conclusion, we have developed a framework to design and study mechanical bilayers with topological polarization in both the in-plane and out-of-plane domains.

The connection between the topologically protected zero modes in spring-mass models and the exponentially localized modes in beam models warrants further study. While the characteristic aspect ratio of the beams serves as an effective parameter for distinguishing between regimes with distinct modal properties, the detailed relation between the topological modes and the beam geometries has yet to be fully characterized. Interestingly, the introduction of beam elements connected at rigid joints not only lifts the frequencies of the edge and bulk modes, but also modifies and hybridizes the spatial features of these modes, thereby opening up new opportunities to control and reconfigure topological mechanical responses via bulk-edge coupling.

Additionally, the statics of mechanical bilayer metamaterials could provide an interesting way to control shape change and provide flexural rigidity. The topological protection of zero modes, as well as their force-bearing counterparts called *states of self stress* [19, 20, 28], means that such structures can offer flexibility or stiffness at designed locations in a manner that is robust against imperfections and fracture [25, 58] which cannot be avoided during fabrication processes. Furthermore, the individual layers possess nonlinear Guest-Hutchinson modes in the spring-mass limit [22, 33], whose interplay with flexural modes may generate Gaussian curvature or changes in the interlayer separation.

IV. MATERIALS AND METHODS

A. Lattice Details

The lattice is 3D printed using selective laser sintering (SLS) technology [59] by Stratasys Direct. The lattice is

first modeled using the Solidworks software and exported as a ".STL" file at a resolution finer than that of the SLS process used (0.76 mm in x– y, and 0.1 mm in z). SLS consists of depositing a fine layer of powder material (Stratasys Nylon 12-glass-fiber-reinforced nylon) which is then melted by a laser into a solid layer following the cross section of a given design, bonding it to all previously deposited layers. This printing process produces a monolithic structure, while the more commonly commercially available fused deposition modeling (FDM) often results in imperfect bonding between deposited layers and adjacent deposited lines that can detrimentally affect wave transport properties. These considerations were key factors in the selection of SLS as the fabrication method for the current task.

The slenderness ratio and cell size are decided concurrently, making sure that the thickness of the beams is within the resolution of the SLS 3D printing process and that the beams are sufficiently slender to prevent their flexural behavior from completely overwhelming the lattice response. The lattice dimensions are selected to be large enough to appreciate the topologically induced decay phenomenon, within the dimensions of the 3D printer's fabrication print bed $(67.31 \times 34.29 \text{ cm})$.

B. Computational Beam Model

The bilayer connections are modeled as 3D Timoshenko beams [57]. We discretized each beam into 9 to 11 elements, depending on the bond length (sufficient discretization for mode visualization), resulting in a model with 3240 and 29376 nodes for the supercell and full-scale lattice models, respectively. For supercell calculations of 100 unit cells, the beams were discretized into only 5 elements due to computational constraints; however, comparing the results of the higher and lower discretization reveals a change of less than 2% for all the relevant modes (lowest 6), meaning that this alternative discretization is accurate in capturing the spectral characteristics of the modes, despite offering a lower spatial resolution of the mode shapes.

Shape functions are used to approximate compatibility relations within one beam element, via interpolation, are used to calculate the elemental dynamical matrix \mathbf{D}_b . These shape functions are linear in axial and torsional deformations, cubic in flexural deformation, and quadratic in rotations - each chosen to be sufficiently differentiable without becoming trivial. Further details can be found in Ref. [57].

C. 3D Laser Doppler Vibrometer Experiments

The experimental setup is shown in Fig. 6. A 3D laser Doppler vibrometer (Polytec PSV-400-3D) is used to measure the velocity of the joints of the beams (the selected scan sites) on the face of the lattice closest to

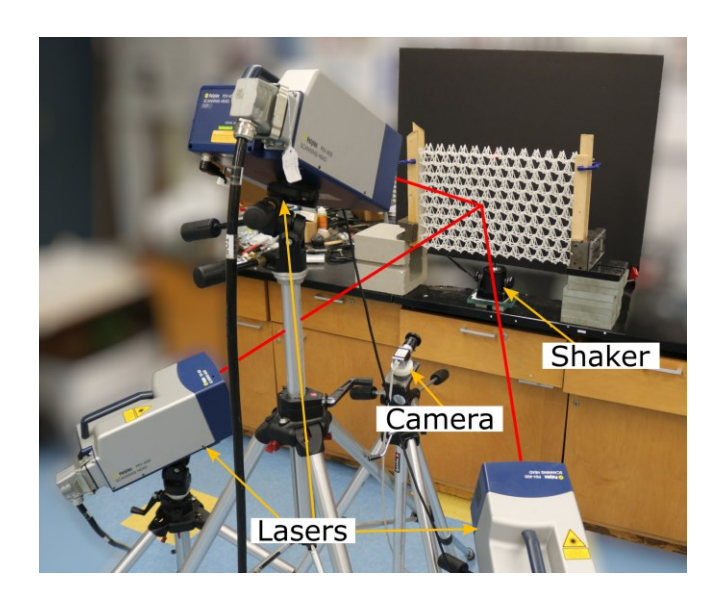


FIG. 6. Experimental setup for the 3D scanning laser Doppler vibrometry (SLDV) testing of the 3D printed bilayer lattice.

the lasers, where reflective tape is applied to increase the material reflectivity, in order to reduce noise in the data. An electromechanical shaker (Brüel & Kjær Type 4810), internally triggered by the vibrometry setup through an amplifier (Brüel & Kjær Type 2718), probes the lattice through a stinger at the desired excitation location, and a 5-cycle Hann-windowed burst, with a carrier frequency

of 300, 900, or 1300 Hz is fired into the structure while velocity is measured by the laser heads at a scan point. The process is repeated for each scan point, automatically moving the lasers to subsequent scan locations in a prescribed sequence, and providing enough relaxation time between scans to ensure bursts have fully dissipated by damping before the next measurement is taken.

The velocity data collected is decomposed into \hat{x} , \hat{y} and \hat{z} components using the Euler angles internally calculated by the vibrometry software. This data is further processed in MATLAB to recreate the wave fields and DFT plots. The temporal data of the spaces between the scan points is interpolated by MATLAB post-processing using a triangulation-based linear interpolation algorithm. It should be noted that this interpolation favors the creation of bulk-appearing wave fronts, which implies that the wave fields for experiments with excitation at the floppy side could potentially be experiencing higher localization than what is shown in the result figures.

ACKNOWLEDGMENTS

This work was supported by the National Science Foundation (NSF Grant No. EFRI-1741618 M.C., S.G.) and the Office of Naval Research (MURI N00014-20-1-2479 J.M., K.S., X.M.) and leveraged the High Performance Computing (HPC) systems at the Minnesota Supercomputing Institute (MSI).

- [1] M. Z. Hasan and C. L. Kane, Colloquium: topological insulators, Reviews of modern physics **82**, 3045 (2010).
- [2] X.-L. Qi and S.-C. Zhang, Topological insulators and superconductors, Reviews of Modern Physics 83, 1057 (2011).
- [3] E. Prodan and C. Prodan, Topological phonon modes and their role in dynamic instability of microtubules, Physical review letters 103, 248101 (2009).
- [4] R. Süsstrunk and S. D. Huber, Observation of phononic helical edge states in a mechanical topological insulator, Science **349**, 47 (2015).
- [5] P. Wang, L. Lu, and K. Bertoldi, Topological phononic crystals with one-way elastic edge waves, Physical review letters 115, 104302 (2015).
- [6] L. M. Nash, D. Kleckner, A. Read, V. Vitelli, A. M. Turner, and W. T. Irvine, Topological mechanics of gyroscopic metamaterials, Proceedings of the National Academy of Sciences 112, 14495 (2015).
- [7] Y.-T. Wang, P.-G. Luan, and S. Zhang, Coriolis force induced topological order for classical mechanical vibrations, New Journal of Physics 17, 073031 (2015).
- [8] J. Ma, K. Sun, and S. Gonella, Valley hall in-plane edge states as building blocks for elastodynamic logic circuits, Physical Review Applied 12, 044015 (2019).
- [9] D. Torrent, D. Mayou, and J. Sanchez-Dehesa, Elastic analog of graphene: Dirac cones and edge states for flexural waves in thin plates, Physical Review B 87, 115143

- (2013).
- [10] S. H. Mousavi, A. B. Khanikaev, and Z. Wang, Topologically protected elastic waves in phononic metamaterials, Nature communications 6, 1 (2015).
- [11] J. Vila, R. K. Pal, and M. Ruzzene, Observation of topological valley modes in an elastic hexagonal lattice, Physical Review B 96, 134307 (2017).
- [12] M. Miniaci, R. Pal, B. Morvan, and M. Ruzzene, Experimental observation of topologically protected helical edge modes in patterned elastic plates, Physical Review X 8, 031074 (2018).
- [13] R. Chaunsali, C.-W. Chen, and J. Yang, Subwavelength and directional control of flexural waves in zone-folding induced topological plates, Physical Review B 97, 054307 (2018).
- [14] R. K. Pal and M. Ruzzene, Edge waves in plates with resonators: an elastic analogue of the quantum valley hall effect, New Journal of Physics 19, 025001 (2017).
- [15] M. Miniaci, R. K. Pal, R. Manna, and M. Ruzzene, Valley-based splitting of topologically protected helical waves in elastic plates, Physical Review B 100, 024304 (2019).
- [16] K. Bertoldi, V. Vitelli, J. Christensen, and M. Van Hecke, Flexible mechanical metamaterials, Nature Reviews Materials 2, 1 (2017).
- [17] X. Li, S. Yu, H. Liu, M. Lu, and Y. Chen, Topological mechanical metamaterials: A brief review, Current

- Opinion in Solid State and Materials Science 24, 100853 (2020).
- [18] C. Kane and T. Lubensky, Topological boundary modes in isostatic lattices, Nature Physics 10, 39 (2014).
- [19] T. Lubensky, C. Kane, X. Mao, A. Souslov, and K. Sun, Phonons and elasticity in critically coordinated lattices, Reports on Progress in Physics 78, 073901 (2015).
- [20] X. Mao and T. C. Lubensky, Maxwell lattices and topological mechanics, Annual Review of Condensed Matter Physics 9, 413 (2018).
- [21] D. Z. Rocklin, Directional mechanical response in the bulk of topological metamaterials, New Journal of Physics 19, 065004 (2017).
- [22] D. Rocklin, S. Zhou, K. Sun, and X. Mao, Transformable topological mechanical metamaterials, Nature communications **8**, 1 (2017).
- [23] O. Stenull, C. Kane, and T. Lubensky, Topological phonons and weyl lines in three dimensions, Physical review letters 117, 068001 (2016).
- [24] J. E. Socolar, T. C. Lubensky, and C. L. Kane, Mechanical graphene, New Journal of Physics 19, 025003 (2017).
- [25] G. Baardink, A. Souslov, J. Paulose, and V. Vitelli, Localizing softness and stress along loops in 3d topological metamaterials, Proceedings of the National Academy of Sciences 115, 489 (2018).
- [26] D. Zhou, L. Zhang, and X. Mao, Topological edge floppy modes in disordered fiber networks, Physical review letters 120, 068003 (2018).
- [27] J. C. Maxwell, L. on the calculation of the equilibrium and stiffness of frames, The London, Edinburgh, and Dublin Philosophical Magazine and Journal of Science 27, 294 (1864).
- [28] C. R. Calladine, Buckminster fuller's "tensegrity" structures and clerk maxwell's rules for the construction of stiff frames, International journal of solids and structures 14, 161 (1978).
- [29] J. Wilhelm and E. Frey, Elasticity of stiff polymer networks, Physical review letters 91, 108103 (2003).
- [30] D. A. Head, A. J. Levine, and F. MacKintosh, Deformation of cross-linked semiflexible polymer networks, Physical review letters **91**, 108102 (2003).
- [31] C. P. Broedersz, X. Mao, T. C. Lubensky, and F. C. MacKintosh, Criticality and isostaticity in fibre networks, Nature Physics 7, 983 (2011).
- [32] D. J. Jacobs and M. F. Thorpe, Generic rigidity percolation: the pebble game, Physical review letters 75, 4051 (1995).
- [33] S. Guest and J. Hutchinson, On the determinacy of repetitive structures, Journal of the Mechanics and Physics of Solids 51, 383 (2003).
- [34] C. S. Borcea and I. Streinu, Periodic frameworks and flexibility, Proceedings of the Royal Society A: Mathematical, Physical and Engineering Sciences 466, 2633 (2010).
- [35] B. G.-g. Chen, N. Upadhyaya, and V. Vitelli, Nonlinear conduction via solitons in a topological mechanical insulator, Proceedings of the National Academy of Sciences 111, 13004 (2014).
- [36] Y. Zhou, B. G.-g. Chen, N. Upadhyaya, V. Vitelli, et al., Kink-antikink asymmetry and impurity interactions in topological mechanical chains, Physical Review E 95, 022202 (2017).
- [37] D. Z. Rocklin, B. G.-g. Chen, M. Falk, V. Vitelli, and T. Lubensky, Mechanical weyl modes in topological maxwell lattices, Physical review letters 116, 135503

- (2016).
- [38] L. D. Landau, E. M. Lifshitz, A. M. Kosevich, and L. P. Pitaevskii, *Theory of elasticity: volume 7*, Vol. 7 (Elsevier, 1986).
- [39] C. D. Santangelo, Extreme mechanics: self-folding origami, Annual Review of Condensed Matter Physics 8, 165 (2017).
- [40] C. D. Santangelo, Theory and practice of origami in science, Soft matter 16, 94 (2020).
- [41] P. Dieleman, N. Vasmel, S. Waitukaitis, and M. van Hecke, Jigsaw puzzle design of pluripotent origami, Nature Physics 16, 63 (2020).
- [42] J. McInerney, B. G.-g. Chen, L. Theran, C. D. Santangelo, and D. Z. Rocklin, Hidden symmetries generate rigid folding mechanisms in periodic origami, Proceedings of the National Academy of Sciences 117, 30252 (2020).
- [43] W. Finbow, E. Ross, and W. Whiteley, The rigidity of spherical frameworks: Swapping blocks and holes, SIAM Journal on Discrete Mathematics 26, 280 (2012).
- [44] B. G.-g. Chen, B. Liu, A. A. Evans, J. Paulose, I. Cohen, V. Vitelli, and C. Santangelo, Topological mechanics of origami and kirigami, Physical review letters 116, 135501 (2016).
- [45] M. Schenk, S. D. Guest, et al., Origami folding: A structural engineering approach, Origami 5, 291 (2011).
- [46] E. Filipov, K. Liu, T. Tachi, M. Schenk, and G. H. Paulino, Bar and hinge models for scalable analysis of origami, International Journal of Solids and Structures 124, 26 (2017).
- [47] M. Charara, K. Sun, X. Mao, and S. Gonella, Topological flexural modes in polarized bilayer lattices, Physical Review Applied 16, 064011 (2021).
- [48] J. Ma, D. Zhou, K. Sun, X. Mao, and S. Gonella, Edge modes and asymmetric wave transport in topological lattices: Experimental characterization at finite frequencies, Physical review letters 121, 094301 (2018).
- [49] A. Souslov, A. J. Liu, and T. C. Lubensky, Elasticity and response in nearly isostatic periodic lattices, Physical review letters 103, 205503 (2009).
- [50] X. Mao, N. Xu, and T. Lubensky, Soft modes and elasticity of nearly isostatic lattices: Randomness and dissipation, Physical review letters 104, 085504 (2010).
- [51] X. Mao and T. C. Lubensky, Coherent potential approximation of random nearly isostatic kagome lattice, Physical Review E 83, 011111 (2011).
- [52] O. Stenull and T. Lubensky, Signatures of topological phonons in superisostatic lattices, Physical review letters 122, 248002 (2019).
- [53] K. Sun and X. Mao, Continuum theory for topological edge soft modes, Physical Review Letters 124, 207601 (2020).
- [54] A. Saremi and Z. Rocklin, Topological elasticity of flexible structures, Physical Review X 10, 011052 (2020).
- [55] M. Stone and P. Goldbart, Mathematics for physics (2002).
- [56] J. N. Goodier and S. Timoshenko, *Theory of elasticity* (McGraw-Hill, 1970).
- [57] H. Karadeniz, M. P. Saka, and V. Togan, Finite element analysis of space frame structures, in *Stochastic Analysis* of Offshore Steel Structures (Springer, 2013) pp. 1–119.
- [58] L. Zhang and X. Mao, Fracturing of topological maxwell lattices, New Journal of Physics 20, 063034 (2018).
- [59] S. Kumar, Selective laser sintering: a qualitative and ob-

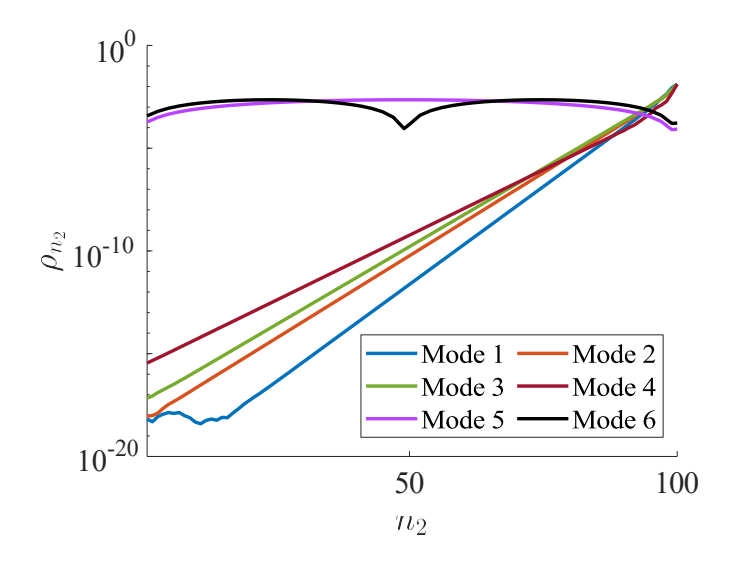


FIG. 7. Displacement vs cell index for 100-cell beam-discretized supercell, showing that, even at much longer supercell lengths, beams with the AR used in the lattice for this work do not produce six modes exhibiting floppy edge localization.

jective approach, Jom 55, 43 (2003).

Appendix A: Flat bands in coplanar Maxwell bilayers

The main text presents mirror-symmetric kagome bilayers with a choice of interlayer connections that exhibit lines of bulk modes in the absence of height modulations within the layers. Here, we present an alternative choice of interlayer connections that instead yields surfaces of bulk modes known as *flat bands*.

The key distinction between coplanar bilayers with lines of bulk zero modes and those with surfaces of bulk zero modes is that the interlayer connections in the former constrain an infinite number of vertices whereas in the latter they constrain a finite number of vertices. For the kagome bilayer, this second condition arises for the following interlayer connections:

$$\mathbf{r}_{1}^{-}(0,0) \longleftrightarrow \mathbf{r}_{2}^{+}(0,0) \longleftrightarrow \mathbf{r}_{3}^{-}(1,-1) \longleftrightarrow \mathbf{r}_{1}^{+}(1,-1) \longleftrightarrow \mathbf{r}_{2}^{-}(0,-1) \longleftrightarrow \mathbf{r}_{3}^{+}(0,-1) \longleftrightarrow \mathbf{r}_{1}^{-}(0,0). \tag{A1}$$

Thus, the vertices can simultaneously displace out-of-plane at any wavevector provided that their displacements are identical to one another:

$$\boldsymbol{\delta}_{1}^{-} = \boldsymbol{\delta}_{2}^{+} = \boldsymbol{\delta}_{3}^{-} e^{-i(\xi_{1} - \xi_{2})} = \boldsymbol{\delta}_{1}^{+} e^{-i(\xi_{1} - \xi_{2})} = \boldsymbol{\delta}_{2}^{-} e^{i\xi_{2}} = \boldsymbol{\delta}_{3}^{+} e^{i\xi_{2}}. \tag{A2}$$

Since such zero modes exist at arbitrary wavevectors, the lowest band is entirely flat. Importantly, the introduction of small height modulations to make the bilayer noncoplanar yields decay rates which cannot be described as a perturbation to the flat band, which makes it more difficult to use this type of connectivity to achieve fully polarized Maxwell bilayers.

Appendix B: Decay Rate for 100-cell Beam-Discretized Supercell

Decay rates for the first six modes of a 100 cell supercell, with AR used in the manufactured lattice, at $\xi = \pi$ are shown in Fig. 7). Here we see that, unlike the low-AR or spring and mass counterparts, modes 5 and 6 remain bulk-like when we increase the supercell to much longer length, revealing that these are not just long decay length modes that simply appear bulk-like due to the relatively short size of the 10-cell supercell. Thus, their residence in the bulk band, as shown in the band diagram, is confirmed.

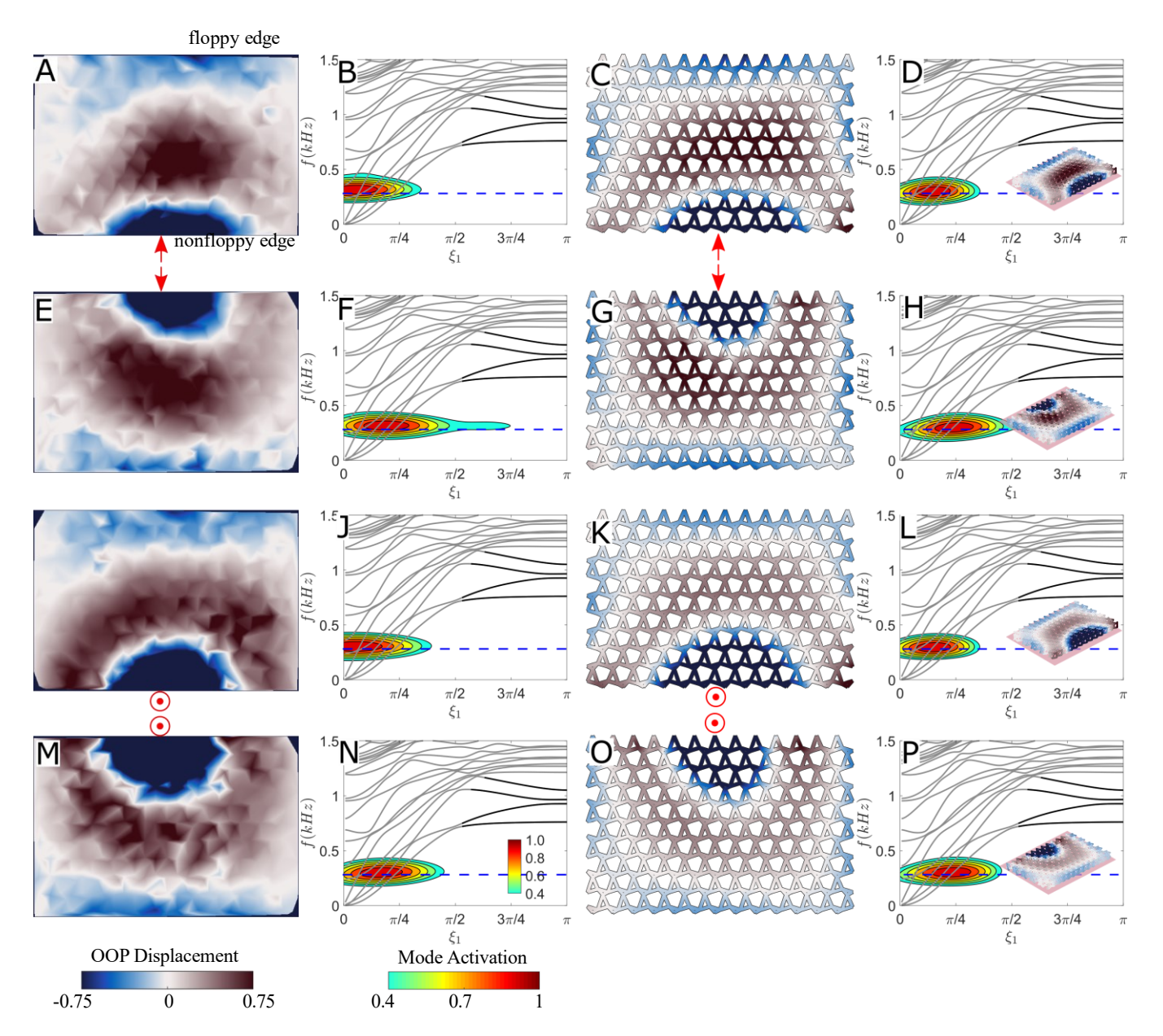


FIG. 8. Wavefield and DFT plots for: experiments (A-B) and simulations (C-D) with an in-plane excitation at the rigid edge, experiments (E-F) and simulations (G-H) with an in-plane excitation at the floppy edge, experiments (I-J) and simulations (K-L) with an out-of-plane excitation at the rigid edge, and experiments (M-N) and simulations (O-P) with an out-of-plane excitation at the floppy edge, all carried out at a carrier frequency of 300 Hz (dashed blue lines). Colorbars in panel M and N apply to all wavefields and contours in the figure, respectively, with the former representing the displacement intensity in the wavefield and the latter highlighting modal activation on the excited edge. While the wavefields capture the signature of wave propagation on the lattice surface, the insets of D, H, L, and P allow to appreciate propagation through the 3D structure of the bilayer. Note that the wavefields and contours are normalized by the highest value in their respective data sets.

Appendix C: Supplemental Results for Experiments and Simulations away from Topological Modes

Wavefield and DFT plots for experiments and simulations at carrier frequencies of 300 and 1300 Hz are shown in Fig.s 8 and 9, respectively. While the main text includes experimental figures highlighting edge-selectivity in the topologically polarized lattice, these images highlight frequency selectivity, an equally important ingredient in ensuring this behavior is not spectrally ubiquitous, providing evidence for the topological nature of the activated modes.

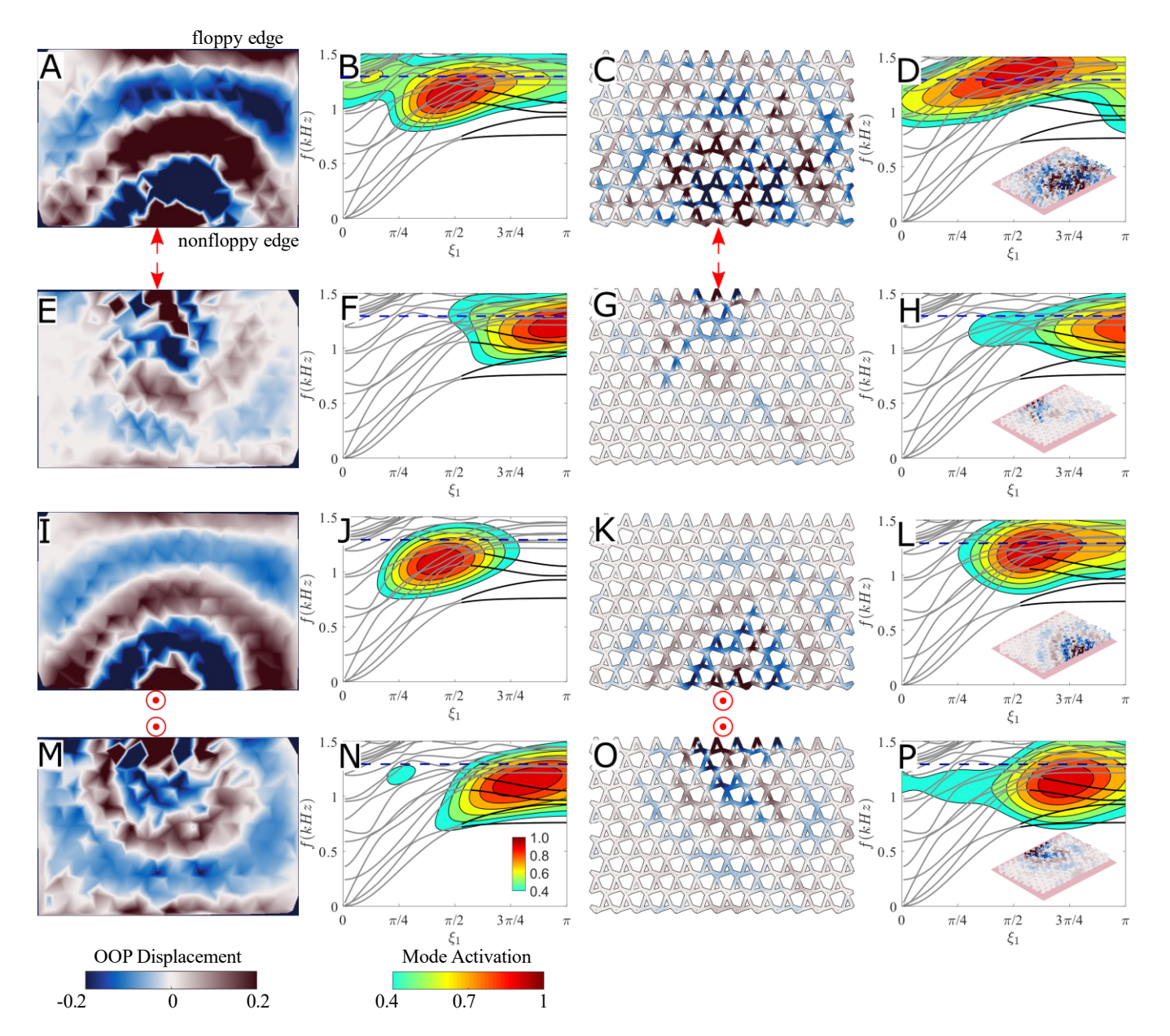


FIG. 9. Wavefield and DFT plots for: experiments (A-B) and simulations (C-D) with an in-plane excitation at the rigid edge, experiments (E-F) and simulations (G-H) with an in-plane excitation at the floppy edge, experiments (I-J) and simulations (K-L) with an out-of-plane excitation at the rigid edge, and experiments (M-N) and simulations (O-P) with an out-of-plane excitation at the floppy edge, all carried out at a carrier frequency of 1300 Hz (dashed blue lines). Colorbars in panel M and N apply to all wavefields and contours in the figure, respectively, with the former representing the displacement intensity in the wavefield and the latter highlighting modal activation on the excited edge. While the wavefields capture the signature of wave propagation on the lattice surface, the insets of D, H, L, and P allow to appreciate propagation through the 3D structure of the bilayer. Note that the wavefields and contours are normalized by the highest value in their respective data sets.

Appendix D: Computational Beam Model: Details

In this work, we choose to work with Timoshenko beams to ensure that the results are robust even for short connections whose slenderness ratio may exceed the bounds for while Euler Bernoulli beam theory is acceptable.

In 3D, the dynamical matrix for a single beam, $\mathbf{D_b}$ (typically referred to as the stiffness matrix \mathbf{K} in structural mechanics, although in this text \mathbf{K} is explicitly used as the diagonal matrix of spring constants in the ideal Maxwell case), encompasses stiffness contributions associated with axial, shear, bending, and torsional deformation. This is captured by reordering rows and columns and partitioning $\mathbf{D_b}$ into minors that highlight the contributions of

different mechanisms. Recalling that $\mathbf{D_b}$ links an array \mathbf{f}_m of nodal forces and moments, to an array $[\mathbf{u}_m \ \boldsymbol{\theta}_m]^T$ of nodal displacements and rotations, the matrix partition can be written as

$$\mathbf{D}_{b_{12\times12}} = \begin{bmatrix} \Box & \mathbf{o} & \mathbf{o} & \mathbf{o} \\ \mathbf{D}_{b_{12\times12}} & \mathbf{o} & \mathbf{D}_{S_{4\times4}} & \mathbf{D}_{M_{4\times6}} \end{bmatrix} .$$

$$\mathbf{o} \quad \mathbf{D}_{M_{4\times6}}^T & \mathbf{D}_B$$
(D1)

where \mathbf{D}_A is the contribution governing axial stiffness, \mathbf{D}_S and \mathbf{D}_B are square matrices controlling shear, and torsion and bending, respectively, and \mathbf{D}_M is a rectangular mixed matrix coupling shear and bending. Note that because the beam element matrices are calculated in a local coordinate system where the \hat{x} axis is along the length of the beam, they must be rotated upon assembly into a global system matrix.

they must be rotated upon assembly into a global system matrix.

As previously mentioned, the dynamical matrix of a beam element is calculated by carrying out the integral $\mathbf{D_b} = {}_L \mathbf{B} \ \mathbf{K_b} \mathbf{B} dL$ over the length of the element. $\mathbf{K_b}$ is diagonal constitutive matrix of elastic coefficients relating

an array σ of stresses and moments to an array c of strains, shears, and curvatures (i.e. $\sigma = \mathbf{K_b}c$) and is given by

$$\mathbf{K}_{b} = \begin{bmatrix} \Box_{EA} & 0 & 0 & 0 & 0 & 0 & \Box \\ 0 & GAk & 0 & 0 & 0 & 0 & \Box \\ 0 & 0 & GAk & 0 & 0 & 0 & \Box \\ 0 & 0 & 0 & GJ & 0 & 0 & \Box \\ 0 & 0 & 0 & 0 & EI & 0 & \Box \\ 0 & 0 & 0 & 0 & 0 & EI & 0 & \Box \end{bmatrix}.$$
(D2)

where E is the Young's Modulus, $A = \pi R^2$ is the cross-sectional area of the beam, I is the second moment of area of the cross section about the y and z axes $(I = \pi R^4/4)$ with R the cross section radius), J is the polar second moment of area of the cross section $(J = \pi R^4/2)$, and k is the area shear correction factor. This matrix features elastic constants for axial deformation (row 1), shear deformation (rows 2 and 3), torsion (row 4), and bending (rows 5 and 6). **B** is an elemental matrix which captures a similar role in a beam element as **C** does in a spring-and-mass bond. **B** contains derivatives of shape functions [that interpolate the elemental displacements and rotations between nodes]. These shape functions are linear in axial and torsional deformation, cubic in flexural deformation, and quadratic in rotations.

As we change the radius of the beam's cross section, the elastic coefficients for axial and flexural deformation scale at different rates - the ratio of the former to the latter is $\propto 1/R^2$. Thus, even though we never lose the inherent effects of clamped boundary conditions and the storage of bending energy of the beams, as we reduce the cross sectional radius R, we asymptotically approach the dominance of axial deformability typical of the spring-mass case.

In the Timoshenko beam framework, the mass matrix of the beam elements is also not diagonal, coupling degrees of freedom in the same manner as $\mathbf{D_b}$. This matrix is calculated by integrating the elemental shape functions, multiplied by material and cross-sectional properties, over the length of the element. The resulting matrix includes contribution from axial, lateral, rotatory (associated with the tilt of the beam cross-sections), and polar (twist about the beam axis) inertial effects. A detailed account of this derivation, as well as that for the beam's dynamical [stiffness] matrix, is provided in ref. [57].